



Engineered bi-functional hydrophilic/hydrophobic yolk@shell architectures: A rational strategy for non-time dependent ultra selective photocatalytic oxidation



Abolfazl Ziarati^a, Alireza Badiei^{a,***}, Rafael Luque^{b,c,*}

^a School of Chemistry, College of Science, University of Tehran, Tehran, Iran

^b Departamento de Química Orgánica, Universidad de Córdoba, Campus de Rabanales, Edificio Marie Curie, E-14014, Córdoba, Spain

^c Peoples Friendship University of Russia (RUDN University), 6 Miklukho-Maklaya str., 117198, Moscow, Russia

ARTICLE INFO

Keywords:
Selective oxidations
Engineered
Photocatalysis
Visible light activation
Bi-functional
Nanoarchitecture

ABSTRACT

Engineered graphene highly wrapped yolk@shell TiO_2 (G-HW-Y@S-TiO_2) architectures were synthesized from fundamental understanding using a multi-step approach as advanced photocatalytic nanomaterials. The resultant G-HW-Y@S-TiO_2 architecture exhibited a superior selective photocatalytic performance in visible light oxidation of aromatic alcohols to corresponding aldehydes (up to 99% in 4 h reaction). Interestingly, the aldehyde was still obtained as single oxidation product after 12 h in presence of G-HW-Y@S-TiO_2 structure. The observed non-time dependent photocatalytic oxidation selectivity can be attributed to the engineered photocatalyst architecture with different hydrophilic level sites between inner core and outer shell that force the hydrophobic aldehyde products to diffuse out from the hydrophilic void space preventing further over-oxidation.

1. Introduction

A major challenge for chemists in the 21st century relates to pollution control and selective transformations via environmentally friendly approaches driven by renewable and clean energy sources [1]. Sunlight stands out as most promising selection to meet energy requirements in chemical processes through its renewable, plentiful and clean features, with a remarkable potential for driving environmentally benign chemical reactions [2–4]. The utilisation of light irradiation could change the thermodynamic emphasis from performing high-temperature chemical transformations to instead favouring chemical reaction at room temperature, avoiding undesirable by-products formation present at higher temperatures [5].

The field of heterogeneous photocatalysis has expanded rapidly in recent years due to various applications [6,7]. Nonetheless, selective organic photosynthetic processes have attracted less attention because of the conventional semiconductor photocatalysts typically have uncontrollable time-dependent oxidation potentials [8–11]. This barrier significantly limits the application of photocatalysts in organic synthesis especially when selective oxidized products are desired. Among them, selective oxidation of aromatic alcohols to corresponding aldehydes is one of the most desirable chemical transformations as the

obtained aldehyde products are important precursors and intermediates for many drugs, vitamins and fragrances [12]. Traditionally, various oxidants including toxic metal oxides, peroxides, halides, ozone, etc., were employed for these selective catalytic oxidation reactions [13,14]. Although this type of oxidation reaction could be achieved with high selectivity and high conversion, these reagents are commonly expensive and could cause serious toxicity issues and environmental pollution. Therefore, the development of an environmental friendly oxidation processes based on rational design of functional photocatalysts with controllable performance and selective/tunable photocatalytic activity is crucially important for applications in selective organic synthesis.

Yolk@shell architectures are a particular class of core@shell structures with specific core@void@shell configuration [15]. These nanostructures feature light-scattering possibilities, reduced diffusion resistance that together with a tuneable developed accessibility may provide a range of various opportunities for photocatalysis [16]. Additionally, the void space existing between the inner core and outer shell can act as nano-reactor and allow the efficient diffusion of reactants, solvents and products through the porous shells [17]. This specialized morphology can be consequently employed to improve the photocatalytic efficiency specially for TiO_2 materials [16,18,19].

Previous reports explored the hydrophilic nature of TiO_2 [20] in

* Corresponding author at: Departamento de Química Orgánica, Universidad de Córdoba, Campus de Rabanales, Edificio Marie Curie, E-14014, Córdoba, Spain.

** Corresponding author at: School of Chemistry, College of Science, University of Tehran, Tehran, Iran.

E-mail addresses: abadiei@khayam.ut.ac.ir (A. Badiei), rafael.luque@uco.es (R. Luque).

order to design further modifications towards bi-functional advanced nanostructures, hybridizing well known hydrophobic carbonaceous materials such as graphene [21–28] with TiO₂ [29–33]. Graphene-wrapping of TiO₂ is a more recent technique to design advanced hybrid titania-graphene nano composites to enhance the electronic contact between graphene sheets and TiO₂ [34,35]. These composites have been shown to provide certain benefits to pure TiO₂ photocatalysis. Firstly, graphene comprises a highly conjugated planar surface which allows a preferential adsorption of aromatic structures such as aromatic alcohols through π–π stacking. Secondly, the addition of graphene has been shown to cause a red-shift in the absorption spectrum leading to titania activation under visible-light irradiation. Third, the presence of two-dimensional graphene significantly improves the charge transport properties of the overall material and decreases the rate of charge carrier recombination owing to its high electron mobility [36].

Various graphene-wrapped TiO₂ nanostructures have been recently reported [37,38]. Nevertheless, these reports generally do not provide improved graphene connecting, light-scattering abilities as well as nanoreactor-like void spaces between inner core and outer shell for diffusional enhancements. Graphene highly wrapped Y@S-TiO₂ architecture with high graphene connecting, excellent surface area and great light-scattering ability is expected not only favour photocatalytic applications, but also act as bi-functional hydrophobic/hydrophilic nanoreactors for ultra-selective photo-oxidation reaction, never reported to date.

In continuation with research endeavours from our groups [39–45], herein we present the design of bi-functional amphiphilic graphene highly wrapped yolk@shell TiO₂ nanoarchitectures as key photocatalysts for an unprecedented non-time dependent ultra-selective photocatalytic oxidation of aromatic alcohols to aldehydes at room temperature under visible light irradiation.

2. Experimental

2.1. Preparation of Y@S-TiO₂

Y@S-TiO₂ structures were prepared according to our previous report [44].

2.2. Preparation of di-amine functionalized Y@S-TiO₂ and amine functionalized Y@S-TiO₂

To increase the electrostatic interaction between Y@S-TiO₂ and GO sheets, di-amine groups were grafted on surface of Y@S-TiO₂. In detail, Y@S-TiO₂ (0.2 g) were dispersed into N-(2-aminoethyl)-3-aminopropyltriethoxysilane (AAPTES) (0.3 mL) in dry toluene solution (100 mL) by sonication. After sonication for 10 min, the suspension was refluxed for 8 h to obtain di-amine functionalized Y@S-TiO₂. Finally, di-amine functionalized Y@S-TiO₂ were sufficiently rinsed with ethanol to wash away any remaining physisorbed AAPTMS moieties. For comparison, the process was repeated with 3-aminopropyltrimethoxysilane (APTES) to produce amine functionalized Y@S-TiO₂.

2.3. Preparation of GO

GO was synthesized from graphite powder according to the modified Hummers method [46].

2.4. Preparation of G-HW-Y@S-TiO₂ and G-W-Y@S-TiO₂

G-HW-Y@S-TiO₂ were prepared by taking advantage of the interaction between di-amine functionalized Y@S-TiO₂ and GO sheets. In a typical process, negatively charged GO suspension in water (0.2 mg mL⁻¹, 20 mL) was added dropwise into high-positively charged di-amine functionalized Y@S-TiO₂ (0.2 g) ethanolic suspension (10 mL), under vigorous stirring at pH 6. The stirring of solution was continued

for 3 h at room temperature, then the obtained suspension was transferred into a Teflon-lined stainless steel autoclave (50 mL capacity) and maintained at 180 °C for 16 h. After that, the mixture was centrifuged and washed with ethanol and dried in 60 °C for 12 h. Finally, the obtain solid was calcined at 400 °C (the heating rate is 3 °C/min) under argon atmosphere for 2 h to remove organic components and gain crystalline G-HW-Y@S-TiO₂. For comparison, the process was repeated with amine functionalized Y@S-TiO₂ to produce G-W-Y@S-TiO₂.

2.5. Preparation of G-W-TiO₂ and G-W-H-TiO₂

G-W-TiO₂ and G-W-H-TiO₂ structures were prepared for comparative purposes according to the literature [35,47].

2.6. Photocatalytic reaction procedures

Visible light photocatalytic reactions were conducted in a parallel photoreaction cells (12 × 5 mL) made of Pyrex glass with continuous O₂ bubbling (10 psi) and water circulation to control the temperature (25 °C) during the experiments. A halogen lamp (Osram, 220 V and 500 W) was used as the visible light source.

For each experiment, 5 mg of catalyst was dispersed in the mixed solution of benzyl alcohol (0.3 mmol) and acetonitrile (3 mL) under continuous O₂ bubbling. Prior to light irradiation, the mixtures were stirred for 1 h in the dark to gain the adsorption – desorption equilibrium for benzyl alcohol and dissolved oxygen on the surface of photocatalyst. The photocatalytic reactions were carried out in 12 parallel reaction cells (To have the same conditions in all reactions) under magnetic stirring in presence of light for 4 h. At the end of reaction, about 1 mL of suspension was withdrawn and centrifuged to remove the remaining catalysts. The concentrations of benzyl alcohols and benzaldehydes were measured with GC-FID or HPLC.

3. Results and discussion

3.1. Photocatalyst preparation and characterizations

Fig. 1 illustrates the multi-step procedure for the preparation of graphene wrapped yolk@shell TiO₂ (G-W-Y@S-TiO₂) and G-HW-Y@S-TiO₂ nanoarchitectures. Y@S-TiO₂ microspheres were prepared via one-pot solvothermal method in presence of Titanium(III) chloride, acetic acid and urea using polyethylene glycol as soft template [16].

Di-amine groups were then introduced to enhance the interaction of the Y@S-TiO₂ with GO sheet, by treating Y@S-TiO₂ with N-(2-aminoethyl)-3-aminopropyltriethoxysilane (AAPTES). Conventional amine treatment of Y@S-TiO₂ was also performed using 3-aminopropyltrimethoxysilane (APTES), as benchmark. [38] GO was subsequently wrapped on the surface of both amine and di-amine functionalized Y@S-TiO₂ microspheres by means of electrostatic attraction interaction between the negatively charged GO sheets and the positively charged functionalized TiO₂ to render graphene wrapped yolk@shell TiO₂ and graphene highly wrapped yolk@shell TiO₂ nanostructures, respectively. G-W-Y@S-TiO₂ and G-HW-Y@S-TiO₂ nanoarchitectures were eventually obtained via hydrothermal treatment and calcination of graphene wrapped yolk@shell TiO₂ and graphene highly wrapped yolk@shell TiO₂. As shown in **Fig. 1** (pathway a), graphene sheets were unable to completely cover Y@S-TiO₂ spheres, whereas the proposed alternative simple wrapping method was able to provide a complete encapsulation of Y@S-TiO₂ with graphene sheets (**Fig. 1**, pathway b).

Fig. 2 shows typical SEM, TEM and HRTEM images of Y@S-TiO₂ (**Fig. 2** (a–d)) and G-HW-Y@S-TiO₂ (**Fig. 2** (e–h)) nanostructures. SEM images of Y@S-TiO₂ at low magnification indicate the presence of monodisperse microspheres with diameter of ca. 2.8 μm (**Fig. 2a**). From the high magnification image of a cracked microsphere (**Fig. 2b**), a solid core inside the shell can be clearly visualized. **Fig. 2c** shows typical TEM images of Y@S-TiO₂ with two magnifications, the gradual contrast of

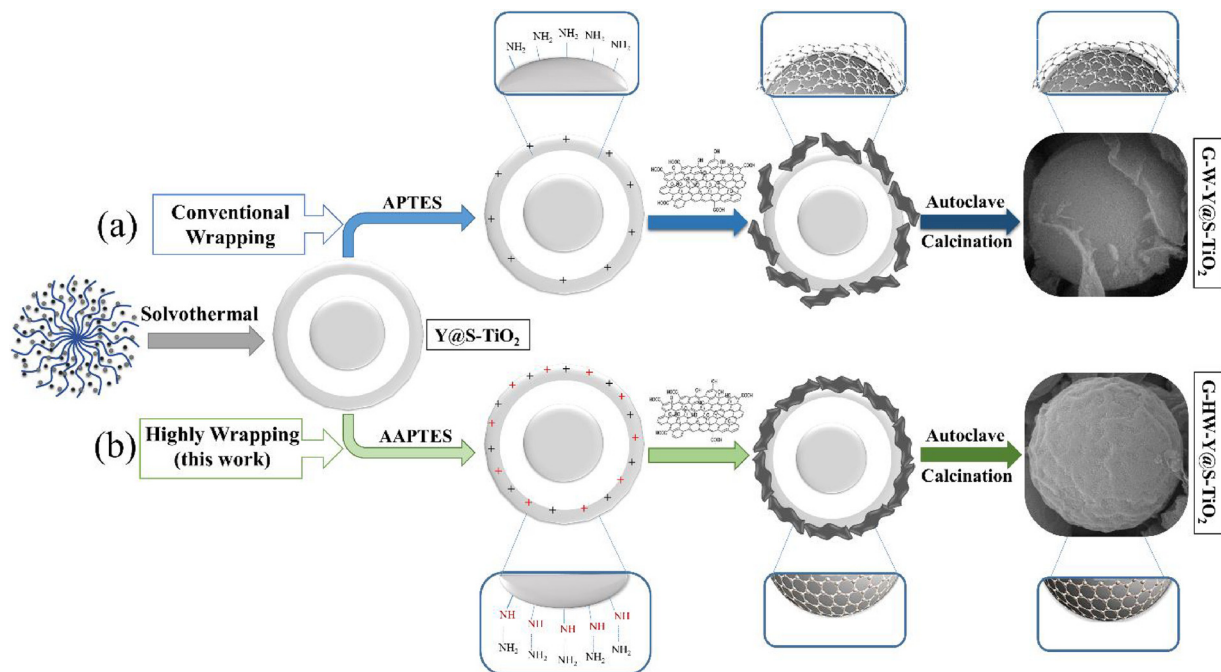


Fig. 1. Overall flowchart for fabrication of the G-W-Y@S-TiO₂ (pathway a) and G-HW-Y@S-TiO₂ (pathway b) architectures.

the TEM image from the edge to the center of the sphere illustrates that the entire sphere is indeed a yolk@shell structure. HRTEM image (Fig. 2d), shows clear lattice fringes with an interplanar distance of 0.35 nm, which corresponds to 101 planes of TiO₂ nanocrystals. Fig. 2 (e–h) displayed SEM, TEM and HRTEM images of G-HW-Y@S-TiO₂. As shown in Fig. 2e, monodisperse G-HW-Y@S-TiO₂ nanoarchitectures were clearly obvious. Fig. 2f shows the high magnification SEM image that pointed to graphene sheets successfully wrapped on the surface of Y@S-TiO₂. Fig. 2g depicts a TEM image of G-HW-Y@S-TiO₂ with different magnifications. The structure of TiO₂ is clearly yolk@shell uniformly covered by graphene sheets. As shown in Fig. 2h, TiO₂ nanocrystals with interplanar distance of 0.35 nm is connected to graphene layers with ca. 5 nm thickness.

In order to investigate the elemental distribution for G-HW-Y@S-

TiO₂ nanoarchitectures, the elemental mappings of C, Ti and O were performed by EDS area scanning (Fig. S1). Mapping of C, Ti and O are well-defined with sharp contrast. In addition, the profile of C is similar to that of Ti and O, which indicates that the graphene sheets are uniformly distributed throughout the whole structure.

X-ray powder diffraction (XRD) was further employed to characterize the crystal structure of C-TiO₂ and G-HW-Y@S-TiO₂ (Fig. S2). Y@S-TiO₂ show a classic XRD pattern of anatase TiO₂ phase according to the standard pattern (JCPDS 21–1272). As expected, XRD patterns of G-HW-Y@S-TiO₂ also include the typical Bragg reflections of anatase TiO₂. In addition, a broad reflection appears around 26°, corresponding to the graphene sheets [48].

Fig. S3 show the Raman spectra of Y@S-TiO₂, GO-HW-Y@S-TiO₂ and G-HW-Y@S-TiO₂, respectively. Four Raman peaks located at

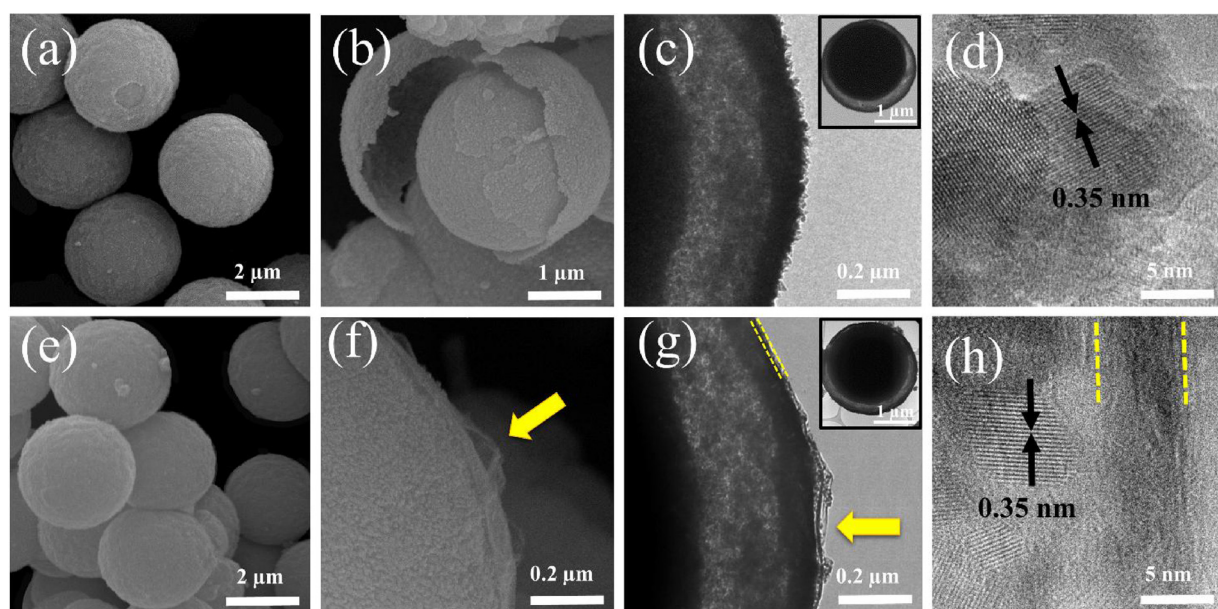


Fig. 2. FESEM, TEM and HRTEM images of the Y@S-TiO₂ (a–d) and G-HW-Y@S-TiO₂ (e–h) architectures. the yellow arrow and lines indicate graphene layers (For interpretation of the references to colour in this figure legend, the reader is referred to the web version of this article).

around 153 cm^{-1} , 401 cm^{-1} , 516 cm^{-1} , 638 cm^{-1} could be observed for Y@S-TiO₂, associated to E_g, B_{1g}, A_{1g} and E_g modes of anatase TiO₂, respectively. For GO two intensity peaks of carbon materials at 1354 cm^{-1} and 1599 cm^{-1} are expected,[49] which are referred as D band (breathing mode of κ -point phonons of A_{1g} symmetry) and G band (E_{2g} phonon of sp² bonds of carbon atoms). All the above mentioned Raman peaks corresponding to GO and TiO₂ are observed in the spectra of GO-HW-Y@S-TiO₂ and G-HW-Y@S-TiO₂. Comparing GO-HW-Y@S-TiO₂ with G-HW-Y@S-TiO₂, an increased value of ID/IG ratio was detected after the hydrothermal treatment and calcination in the Raman spectra, related to the reduction of GO. After these thermal processes, oxygen functional groups in GO sheets were reduced and the conjugated G network (sp² carbon) will be re-established, which would lead to an increase in the ID/IG ratio [49].

Fig. S4 presents the FTIR spectra of Y@S-TiO₂, di-amine functionalized Y@S-TiO₂, GO and G-HW-Y@S-TiO₂. Peaks at $\sim 700\text{ cm}^{-1}$ present in Y@S-TiO₂, di-amine functionalized Y@S-TiO₂ and G-HW-Y@S-TiO₂ samples can be assigned to Ti–O–Ti stretching vibrations. The bands at $\sim 2940\text{ cm}^{-1}$ and 2850 cm^{-1} confirmed the presence of aliphatic hydrocarbon groups in di-amine functionalized Y@S-TiO₂. Moreover, the band located at 3360 cm^{-1} and 3400 cm^{-1} corresponded to the stretching vibration of di-amine groups. In the spectra of GO, the nearly broad band upper 3000 cm^{-1} was ascribed to the stretching vibration of O–H. The two bands at 1731 cm^{-1} and 1623 cm^{-1} were attributed to the stretching vibrations of C=O of carboxylic groups and C=C, respectively. The absorption peak at 1064 cm^{-1} is attributed to the C–O–C stretching vibrations. G-HW-Y@S-TiO₂ sample shows two characteristic peaks at 1550 cm^{-1} and 1690 cm^{-1} for CNH stretch and CNO amide group. These peaks indicate the presence of the covalent bonds formed during the wrapping process.

To further confirm the chemical compositions of G-HW-Y@S-TiO₂ nanoarchitectures, XPS measurements were conducted. According to Fig. 3a, the spectra displayed the existence of Ti, O and C. The high-resolution XPS spectra (Fig. 3 (b, c)) indicate the binding energies and chemical bonds of C 1s and Ti 2p. As can be seen from Fig. 3b, C 1s peak located at 284.6 eV can be assigned to carbon in the graphene state. Moreover, the detected peaks located at binding energies of 286.1 eV and 288.2 eV could be attributed to C–O and C=O bands, respectively [50]. The spin orbit components ($2p_{3/2}$ and $2p_{1/2}$) of Ti 2p peak (Fig. 3(c)) were present at 458.2 eV and 464.4 eV , respectively, assigned to Ti⁴⁺ in the TiO₂ lattice.

The optical absorption of commercial TiO₂ (C-TiO₂) and G-HW-Y@S-TiO₂ were determined with diffuse reflectance UV-vis spectroscopy and compared in Fig. S5a. A classic semiconductor absorption property was observed for C-TiO₂, which has a strong absorption in the ultraviolet region and lower absorption in the visible light region. Comparatively, the absorption intensity in the visible region was much improved for G-HW-Y@S-TiO₂ microspheres, which may be attributable to the effective graphene wrapping process on the Y@S-TiO₂ surface. Furthermore, the bandgap of the C-TiO₂ and G-HW-Y@S-TiO₂ were calculated to 3.2 eV and 2.6 eV , respectively (Fig. S5b). These

results pointed out that G-HW-Y@S-TiO₂ architectures could be well excited under visible light irradiation.

The measurement of photoluminescence (PL) spectra has been widely accepted to characterize the charge recombination rate of photocatalysts because of the PL emission is originated from the recombination of photo-generated electrons and holes. PL spectra of Y@S-TiO₂ and G-HW-Y@S-TiO₂ structures in the wavelength range of 350 – 600 nm with excitation at 320 nm are shown in Fig. S6 (see Supporting Information). PL intensities for G-HW-Y@S-TiO₂ decrease as compared to Y@S-TiO₂. This result indicated that the recombination rate of photogenerated electrons and holes had been considerably inhibited in G-HW-Y@S-TiO₂ architectures because the electrons excited from CB of Y@S-TiO₂ were injected into the carbon scaffold in wrapped graphene. The effective charge carrier separation extended the reactive electron and hole lifetimes and accordingly enhanced the photocatalytic activity of the photocatalysts.

To obtain further insights into the porous wrapped yolk@shell structure, the pore-size distributions and BET surface areas of G-HW-Y@S-TiO₂ nanoarchitectures were measured using N₂ adsorption and desorption isotherms (Fig. S7 (a, b)). Y@S-TiO₂ and C-TiO₂ were also tested here as benchmark. BET surface area of G-HW-Y@S-TiO₂ was significant ($195\text{ m}^2\cdot\text{g}^{-1}$), ca. five times larger than that of C-TiO₂ ($41\text{ m}^2\cdot\text{g}^{-1}$) and slightly superior to that of Y@S-TiO₂ ($181\text{ m}^2\cdot\text{g}^{-1}$). Such increase in surface area may be attributed to the contribution of graphene sheets on porous yolk@shell architectures. Isotherms corresponding to G-HW-Y@S-TiO₂ displayed typical type IV curves according to the IUPAC classification, with a hysteresis loop at high relatively pressures associated with capillary condensation of gases within mesoporous. The pore size distribution (Fig. S7b) calculated from the adsorption branch of the nitrogen isotherm by the BJH method shows a relatively narrow range from 2 to 10 nm .

3.2. Photocatalytic activity

The engineered graphene highly wrapped yolk@shell nanoarchitectures with high surface area, bi-functional hydrophobic/hydrophilic structure as well as visible light activation properties make G-HW-Y@S-TiO₂ microspheres ideal candidates for selective photocatalytic applications. The photocatalytic performance of G-HW-Y@S-TiO₂ was tested in the visible light selective photo-oxidation of benzyl alcohol. Graphene wrapped TiO₂ (G-W-TiO₂), graphene wrapped hollow TiO₂ (G-W-H-TiO₂) and G-W-Y@S-TiO₂ microspheres were also tested here as benchmark (Fig. 4).

The visible light photocatalytic conversion and selectivity of G-W-TiO₂ were disappointingly only moderate (47% and 61%, respectively). When the oxidation reaction was carried out in the presence of G-W-H-TiO₂ microspheres, the photocatalytic activity could be pushed to 78% conversion at 94% selectivity to benzaldehyde. Gratifyingly, both G-W-Y@S-TiO₂ and G-HW-Y@S-TiO₂ exhibited excellent photocatalytic activities under identical reaction conditions (> 90%, > 99% selectivity).

The excellent photocatalytic activities of G-W-Y@S-TiO₂ and G-HW-

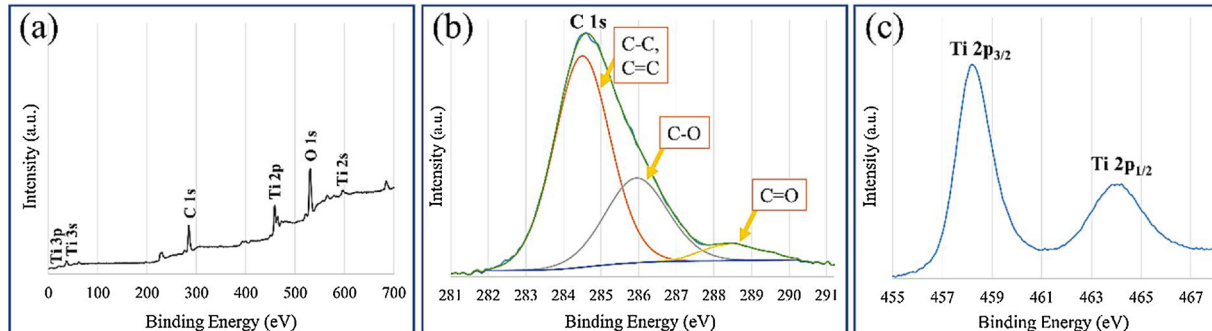


Fig. 3. XPS survey spectrum (a), high resolution C 1s spectrum (b) and high resolution Ti 2p spectrum (c) G-HW-Y@S-TiO₂ architecture.

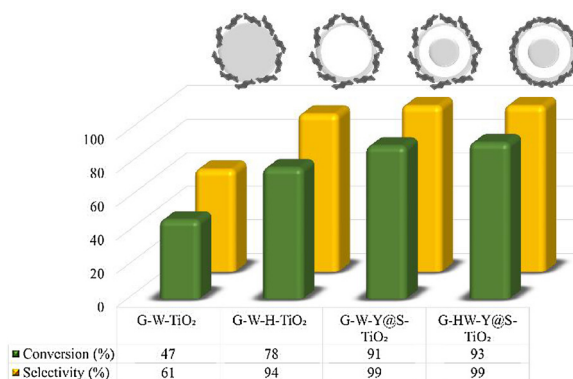


Fig. 4. Comparison photocatalytic activity of G-W-TiO₂, G-W-H-TiO₂, G-W-Y@S-TiO₂ and G-HW-Y@S-TiO₂ structures in photocatalytic benzyl alcohol oxidation.

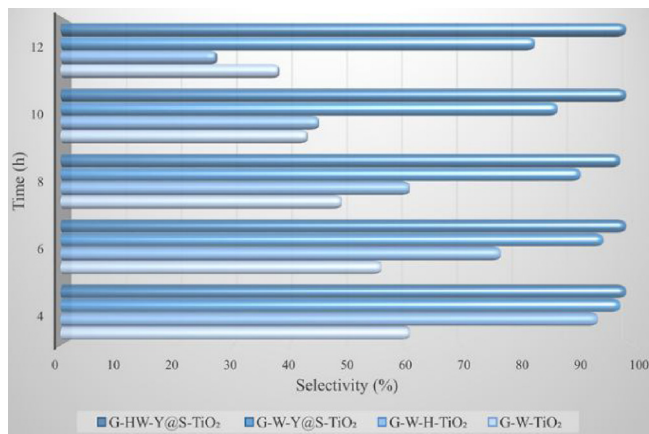


Fig. 5. Time dependent photocatalytic selectivity of G-W-TiO₂, G-W-H-TiO₂, G-W-Y@S-TiO₂ and G-HW-Y@S-TiO₂ structures in photocatalytic benzyl alcohol oxidation.

Y@S-TiO₂ may be attributed to a number of phenomena occurring in these structures under visible light irradiation: 1) reflecting and scattering of light between inner core and outer shell in yolk@shell architectures which improves light harvesting; 2) high porosity and void space in the structures, beneficial for the transportation and adsorption of organic molecules thus, accelerating the catalytic process; 3) the presence of ultrathin shells, which enable a maximized molecular diffusion and make active sites highly exposed to reactants 4) the conjugated planar graphene on Y@S-TiO₂ surface which allows preferential adsorption of aromatic compounds such as aromatic alcohols through II-II stacking; 5) the wrapping of graphene sheets on the surface of TiO₂ shell which reduce the band gap of TiO₂ to the visible region; 6) the high electron mobility in wrapped graphene structures that greatly improves charge transport properties and reduces the rate of charge carrier recombination. Time-dependent experiments were subsequently carried out to provide additional insights into reaction selectivity (Fig. 5).

Unexpectedly, longer times of reaction in the photo-oxidation process catalysed by G-HW-Y@S-TiO₂ (up to 12 h) did not change the selectivity to over oxidation products (such as benzoic acid, observed in considerable quantities for G-W-TiO₂). Indeed, prolonged times of reaction decreased the photo-oxidation yields to 83% for G-W-Y@S-TiO₂, with gradually increased observation of over-oxidation products. The decreasing in selectivity value was significantly larger for G-W-TiO₂ and G-W-H-TiO₂ (aldehyde selectivity only 27% and 38%, respectively, after 12 h visible light irradiation)

The suggested reasons of such unprecedented selective for G-HW-

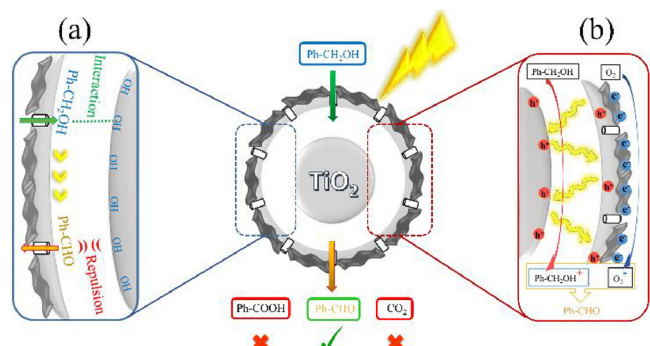


Fig. 6. Schematic diagram of the selective oxidation performance caused by bi-functional hydrophobic/hydrophilic G-HW-Y@S-TiO₂ (a) and schematic of the proposed mechanism for selective alcohol oxidation by G-HW-Y@S-TiO₂ (b).

Y@S-TiO₂ in benzyl alcohol oxidation may be attributed to the bi-functional yolk@shell features of this engineered system. G-HW-Y@S-TiO₂ not only provided a void space among inner core and outer shell (potentially acting as “nanoreactor”), but also specially separated the two hydrophobic carbonaceous shell and hydrophilic titania core active sites.

As illustrated in Fig. 6a, the alcohol reactants pass through the outer mesoporous shell to reach the inner hydroxyl rich titanium oxide core. The photocatalytic oxidation reactions were confined within this void space among core and shell. After photocatalytic conversion of relatively hydrophilic alcohols to relatively hydrophobic aldehydes, hydrophobic/hydrophilic repulsions between aldehyde products and TiO₂ core are forcing the aldehyde to diffuse out from the inner void space of the photocatalyst through the outer shell prior to undergoing over-oxidation. After diffusing-out, the completely graphene covered shell in G-HW-Y@S-TiO₂ prevented further contact of the aldehyde intermediate with photogenerated h⁺ left in TiO₂ and therefore over-oxidation reactions did not take place even under prolonged time of reaction. Interestingly, such remarkable phenomena were only partially suppressed in G-W-Y@S-TiO₂ partially graphene-covered materials. At longer times of visible light irradiation, there is a certain probability of random collisions between aldehyde intermediates and partially uncovered h⁺ rich TiO₂ shell, with over-oxidation products generated to a certain extend. Comparatively, G-W-H-TiO₂ is completely different since the hydrophilic core does not exist and the aldehyde molecules are not in principle pushed to diffuse out upon reaction. Consequently, the aldehydes are present in higher concentration in the hollow spheres and over-oxidation reactions progressed. Last, but not least, the observed over-oxidation present in G-W-TiO₂ could be attributed to the collision between substrates and catalyst in the absence of inner core/outer shell void space in the system. These findings pointed out the importance of a rational design of (photo) nanocatalysts based on fundamental understanding to render advanced functional materials (G-HW-Y@S-TiO₂) for targeted applications.

To understand the primary reactive species involved in the selective oxidation of benzyl alcohol over G-HW-Y@S-TiO₂ under visible light irradiation, we performed a series of control experiments under N₂ atmosphere or in the presence of different radical scavengers. Here, benzoquinone (BQ) was introduced to scavenge ·O₂⁻, ammonium oxalate (AO) for h⁺, and t-BuOH for ·OH in the solution, each with a concentration of 2 mM [51,52]. As shown in Fig. S8, in N₂ atmosphere, the conversion of benzyl alcohol is completely negligible, implying that oxygen is an essential oxidant substance in the photocatalytic oxidation. The addition of BQ drastically decreased the conversion rate of benzyl alcohol, indicating that ·O₂⁻ is an important reactive species for benzyl alcohol oxidation. A similar inhibition effect is observed with the introduction of AO, manifesting that the photogenerated holes are also involved in the oxidation of benzyl alcohol. However, the addition

Table 1
Photocatalytic selective oxidation of Alcohols with the G-HW-Y@S-TiO₂ ^a.

R	t[h]	Conversion (%)	Selectivity (%)
H	4	93	99
4-Me	4	88	99
3-Me	4	86	99
4-OMe	4	90	98
4-NO ₂	4	89	98
4-Cl	4	90	97
2-Cl	4	86	97

^a Reaction conditions: photocatalyst (5 mg), alcohol (0.3 mmol), O₂ bubbling, acetonitrile (3 mL), 298 K.

of t-BuOH almost has no influence on the conversion rate of benzyl alcohol, proving that ·OH is not the reactive species for benzyl alcohol oxidation. Based on the above experiment results, we can infer that in this reaction system ·O₂[−] and hole are the main reactive species for benzyl alcohol oxidation.

The suggested photocatalytic mechanism of G-HW-Y@S-TiO₂ has been fully depicted in Fig. 6b. When light is irradiated on the G-HW-Y@S-TiO₂ surface, electrons are photo-excited to the conduction band of TiO₂, leaving positive charged holes in the valence band. According to the literature, typical work functions of graphene and TiO₂ are 4.42 eV and 4.21 eV, respectively [53]. This explained that, graphene can receive the photo-excited electrons from TiO₂, thus prevents the electron–hole recombination. The photo-generated h⁺ left in TiO₂ valence band can transfer to alcohol substrates to produce benzyl alcohol cation radicals, and the excited e[−] stored in GO can activate the dissolved O₂ to form the ·O₂[−] radicals. Finally, the benzyl alcohol cation radicals can react with the ·O₂[−] radicals to yield benzaldehyde.

Therefore, such an engineered graphene highly wrapped yolk@shell structure with hydrophilic sites at the core and hydrophobic sites at the shell ensured that the visible light oxidation reaction of alcohols were selective with high yield and aldehyde species were left the catalyst before they converted to acids or CO₂. This strategy is leading to excellent activity and selectivity of visible light photocatalytic oxidation toward the target aldehyde product during the whole catalytic reaction process.

The scope of the oxidation reaction was studied using various aromatic alcohols and the results are summarized in Table 1.

3.3. Reusability tests

The recovery and reusability of G-HW-Y@S-TiO₂ structure was also investigated for the photocatalytic selective oxidation of benzyl alcohol. In each run, the photocatalyst was recycled and then washed with hot ethanol several times. After drying, G-HW-Y@S-TiO₂ was reused in the photocatalytic reaction. Interestingly, this architecture exhibited excelling photocatalytic activity and selectivity after several uses (five consecutive runs), with an almost negligible decrease in conversion and selectivity (Fig. S9). This outstanding durability can be attributed to the engineered structure of G-HW-Y@S-TiO₂ with robust wrapping within graphene sheets.

4. Conclusions

In conclusion, innovative G-HW-Y@S-TiO₂ nanoarchitectures were synthesized from fundamental understanding using a multi-step approach as advanced photocatalytic nanomaterials. Optimised nanomaterials exhibited an unprecedented photocatalytic performance in

visible light oxidation of aromatic alcohols (up to 99% to the respective aldehydes, 4 h reaction), with a remarkable selectivity to the aldehydes as single oxidation products after 12 h. This non-time dependent photocatalytic oxidation selectivity can be attributed to the engineered photocatalyst architecture with different hydrophilic level sites between inner core and outer shell that force the hydrophobic aldehyde products to diffuse out from the hydrophilic void space preventing further over-oxidation. The proposed systems may pave the way to a more extended utilisation of engineered advanced nanocatalysts for selective photocatalytic processes that will be reported in due course.

Acknowledgements

The authors thank University of Tehran (Iran) and funding from Universidad de Cordoba (Programa Propio), Spain. The publication has been prepared with support from RUDN University Program 5-100 (Russia).

Appendix A. Supplementary data

Supplementary data associated with this article can be found, in the online version, at <https://doi.org/10.1016/j.apcatb.2018.08.058>.

References

- [1] P. Anastas, N. Eghbali, Chem. Soc. Rev. 39 (2010) 301–312.
- [2] L.V. Bora, R.K. Mewada, Renew. Sust. Energy Rev. 76 (2017) 1393–1421.
- [3] S.J. Moniz, S.A. Shevlin, D.J. Martin, Z.X. Guo, J. Tang, Energy Environ. Sci. 8 (2015) 731–759.
- [4] D.M. Schultz, T.P. Yoon, Science 343 (2014) 1239176.
- [5] B.H. Nguyen, A. Redden, K.D. Moeller, Green Chem. 16 (2014) 69–72.
- [6] X. Lang, X. Chen, J. Zhao, Chem. Soc. Rev. 43 (2014) 473–486.
- [7] A. Studer, D.P. Curran, Nat. Chem. 6 (2014) 765.
- [8] Q. Xiao, E. Jaatinen, H. Zhu, Chem. Asian J. 9 (2014) 3046–3064.
- [9] B. König, Eur. J. Org. Chem. 2017 (2017) 1979–1981.
- [10] Y. Dai, C. Li, Y. Shen, T. Lim, J. Xu, Y. Li, H. Niemantsverdriet, F. Besenbacher, N. Lock, R. Su, Nat. Commun. 9 (2018) 60.
- [11] X. Zhang, X. Li, D. Zhang, N.Q. Su, W. Yang, H.O. Everitt, J. Liu, Nat. Commun. 8 (2017) 14542.
- [12] G.J. ten Brink, I.W. Arends, R.A. Sheldon, Science 287 (2000) 1636–1639.
- [13] T. Mallat, A. Baiker, Chem. Rev. 104 (2004) 3037–3058.
- [14] M. Besson, P. Gallozot, Catal. Today 57 (2000) 127–141.
- [15] R. Purbia, S. Paria, Nanoscale 7 (2015) 19789–19873.
- [16] J. Feng, Y. Hong, J. Zhang, P. Wang, Z. Hu, Q. Wang, L. Han, Y. Zhu, J. Mater. Chem. A Mater. Energy Sustain. 2 (2014) 1502–1508.
- [17] J. Liu, S.Z. Qiao, J.S. Chen, X.W.D. Lou, X. Xing, G.Q.M. Lu, ChemComm 47 (2011) 12578–12591.
- [18] Z. Jiang, C. Zhu, W. Wan, K. Qian, J. Xie, J. Mater. Chem. A Mater. Energy Sustain. 4 (2016) 1806–1818.
- [19] Z.Q. Li, W.C. Chen, F.L. Guo, L.E. Mo, L.H. Hu, S.Y. Dai, Sci. Rep. 5 (2015).
- [20] N. Stevens, C.I. Priest, R. Sede, J. Ralston, Langmuir 19 (2003) 3272–3275.
- [21] F. Taherian, V. Marcon, N.F. van der Vegt, F. Leroy, Langmuir 29 (2013) 1457–1465.
- [22] W. Cui, J. He, H. Wang, J. Hu, L. Liu, Y. Liang, Appl. Catal. B-Environ. 232 (2018) 232–245.
- [23] Y. Zhang, W. Cui, W. An, L. Liu, Y. Liang, Y. Zhu, Appl. Catal. B-Environ. 221 (2018) 36–46.
- [24] F. Chen, W. An, L. Liu, Y. Liang, W. Cui, Appl. Catal. B-Environ. 217 (2017) 65–80.
- [25] X. Wang, Y. Liang, W. An, J. Hu, Y. Zhu, W. Cui, Appl. Catal. B-Environ. 219 (2017) 53–62.
- [26] H. Wang, Y. Liang, L. Liu, J. Hu, P. Wu, W. Cui, Appl. Catal. B-Environ. 208 (2017) 22–34.
- [27] C. Mu, Y. Zhang, W. Cui, Y. Liang, Y. Zhu, Appl. Catal. B-Environ. 212 (2017) 41–49.
- [28] Y. Li, W. Cui, L. Liu, R. Zong, W. Yao, Y. Liang, Y. Zhu, Appl. Catal. B-Environ. 199 (2016) 412–423.
- [29] B. Bhanvase, T. Shende, S. Sonawane, Environ. Technol. Rev. 6 (2017) 1–14.
- [30] J. Yang, Z. Wen, X. Shen, J. Dai, Y. Li, Y. Li, Chem. Eng. J. 334 (2018) 907–921.
- [31] N. Khalid, A. Majid, M.B. Tahir, N. Niaz, S. Khalid, Ceram. Int. 43 (2017) 14552–14571.
- [32] L. Chen, F. Chen, Y. Shi, J. Zhang, J. Phys. Chem. C 116 (2012) 8579–8586.
- [33] R. Leary, A. Westwood, Carbon 49 (2011) 741–772.
- [34] G. Lui, J.Y. Liao, A. Duan, Z. Zhang, M. Fowler, A. Yu, J. Mater. Chem. A Mater. Energy Sustain. 1 (2013) 12255–12262.
- [35] X. Yan, Y. Li, F. Du, K. Zhu, Y. Zhang, A. Su, G. Chen, Y. Wei, Nanoscale 6 (2014) 4108–4116.
- [36] C. Han, N. Zhang, Y.J. Xu, Nano Today 11 (2016) 351–372.
- [37] J.S. Lee, K.H. You, C.B. Park, Adv. Mater. 24 (2012) 1084–1088.

[38] C. Wang, D. Meng, J. Sun, J. Memon, Y. Huang, J. Geng, *Adv. Mater. Interfaces* 1 (2014) 1300150.

[39] J. Poostforooshan, A. Badiei, M. Kolahdouz, A.P. Weber, *ACS Appl. Mater. Interfaces* 8 (2016) 21731–21741.

[40] S. De, J. Zhang, R. Luque, N. Yan, *Energy Environ. Sci.* 9 (2016) 3314–3347.

[41] H. Eskandarloo, M. Hashempour, A. Vicenzo, S. Franz, A. Badiei, M.A. Behnajady, M. Bestetti, *Appl. Catal. B-Environ.* 185 (2016) 119–132.

[42] A. Ziarati, A. Badiei, G. Mohammadi Ziarani, H. Eskandarloo, *Catal. Commun.* 95 (2017) 77–82.

[43] J.C. Colmenares, W. Ouyang, M. Ojeda, E. Kuna, O. Chernyyayeva, D. Lisoviytskiy, S. De, R. Luque, A.M. Balu, *Appl. Catal. B-Environ.* 183 (2016) 107–112.

[44] A. Ziarati, A. Badiei, R. Luque, W. Ouyang, *J. Mater. Chem. A Mater. Energy Sustain.* 6 (2018) 8962–8968.

[45] A. Ziarati, A. Badiei, R. Luque, *Appl. Catal. B-Environ.* 238 (2018) 177–183.

[46] Y. Xu, H. Bai, G. Lu, C. Li, G. Shi, *J. Am. Chem. Soc.* 130 (2008) 5856–5857.

[47] J. Zhang, Z. Zhu, Y. Tang, X. Feng, *J. Mater. Chem. A Mater. Energy Sustain.* 1 (2013) 3752–3756.

[48] L. Gu, H. Zhang, Z. Jiao, M. Li, M. Wu, Y. Lei, *RSC Adv.* 6 (2016) 67039–67048.

[49] H. Liu, T. Lv, Z. Zhu, *J. Mol. Catal. A-Chem.* 404 (2015) 178–185.

[50] D. Chen, L. Zou, S. Li, F. Zheng, *Sci. Rep.* 6 (2016) 20335.

[51] X. Yang, J. Qin, Y. Jiang, K. Chen, X. Yan, D. Zhang, R. Li, H. Tang, *Appl. Catal. B-Environ.* 166 (2015) 231–240.

[52] M.Q. Yang, N. Zhang, Y.J. Xu, *ACS Appl. Mater. Interfaces* 5 (2013) 1156–1164.

[53] Y. Liu, D. Zhang, Y. Shang, W. Zang, M. Li, *RSC Adv.* 5 (2015) 104785–104791.